JGR Space Physics

RESEARCH ARTICLE

Key Points:
- We demonstrate reconstructing the three-dimensional shape of the magnetopause and bow shock from single two-dimensional images
- In our simulations the reconstruction is not strongly dependent on viewing geometry
- The reconstruction algorithm is successful for low count rates, less than one per pixel

Correspondence to:
T. Sun,
trsun@spaceweather.ac.cn

Boundary Detection in Three Dimensions With Application to the SMILE Mission: The Effect of Photon Noise

Anders M. Jorgensen[1] , **Tianran Sun[2]** , **Chi Wang[2]** , **Lei Dai[2]** , **Steven Sembay[3]** , **Fei Wei[2]** , **Yihong Guo[2]** , and **Ronglan Xu[2]**

[1]Electrical Engineering Department, New Mexico Institute of Mining and Technology, Socorro, NM, USA, [2]State Key Laboratory of Space Weather, National Space Science Center, Chinese Academy of Sciences, Beijing, China, [3]Department of Physics and Astronomy, University of Leicester, Leicester, UK

Abstract Imaging magnetospheric satellite missions provide information, which is complementary to in situ observations. Imaging is often able to provide an instantaneous picture of large-scale structures, whereas in situ measurements, even multipoint in situ measurements, can only provide an average view of large-scale structure. But imaging also presents some challenges. When three-dimensional structures need to be extracted from two-dimensional images, it is necessary to either make suitable assumptions or record a large enough number of images from different viewing geometries to allow a reconstruction (e.g., tomography). Imaging data exist over a wide range of sources including visible light, ultraviolet light, extreme ultraviolet, energetic neutral atoms, and X-rays, each informing different physical mechanisms. In this paper we consider the extraction of the geometry of the magnetopause and the bow shock from single X-ray images expected from the Solar wind Magnetosphere Ionosphere Link Explorer (SMILE) mission. We examine the effect of photon-counting noise in determining the boundary geometries. We also consider the effect of different viewing geometries in the form of orbital vantage point and target look direction. Finally, we consider the effect of background noise. We find that our approach is relatively robust to viewing geometry effects and works at low count rates.

1. Introduction

The Earth's magnetosheath is luminous in the soft X-ray band, predicted by the solar wind charge exchange (SWCX) mechanism. SWCX was first proposed by Cravens (1997) to explain observations of X-ray emissions from the comet Hyakutake (Lisse et al., 1996). SWCX occurs when highly ionized solar wind species encounter the neutral atoms such as the exospheric (geocoronal) hydrogen. During this process, the solar wind ions capture electrons initially into an excited state and then decay to the ground state accompanied by photon emissions. These highly ionized ions originate in the solar atmosphere and, for the most part, do not enter the magnetospheric cavity and thus are primarily only present in the magnetosheath, cusps, and solar wind. The magnetospheric plasma originating in the Earth's atmosphere does not contain highly ionized ions because of its lower temperature. Also, plasma does not readily cross the magnetopause. The result is emissions of X-rays outside of the magnetopause and barely any emissions inside the magnetopause, creating a sharp boundary. Furthermore, the solar wind density, velocity, and temperature change at the bow shock, which thus produces a change of the X-ray emission at the bow shock as well. Therefore, images of the magnetosheath can provide information of the magnetopause and bow shock positions. SWCX emissions from the magnetosheath have been confirmed by observations from astronomical missions (e.g., Carter et al., 2010; Snowden et al., 2009). Nevertheless, imaging of the large-scale magnetosheath via a telescope with wide field of view (FOV) is still missing. And this is the aim of the Solar wind Magnetosphere Ionosphere Link Explorer (SMILE) mission (Raab et al., 2016).

SMILE is a joint mission between the European Space Agency and the Chinese Academy of Sciences, planned to be launched in the 2022–2023 time frame. It will observe solar wind-magnetosphere-ionosphere coupling via simultaneous in situ detection of the solar wind/magnetosheath plasma and magnetic field, soft X-ray images of the magnetosheath and cusps, and ultraviolet images of the global auroral distributions. The payloads on board SMILE will include a Soft X-ray Imager (SXI), UltraViolet Imager, Light Ion Analyser,
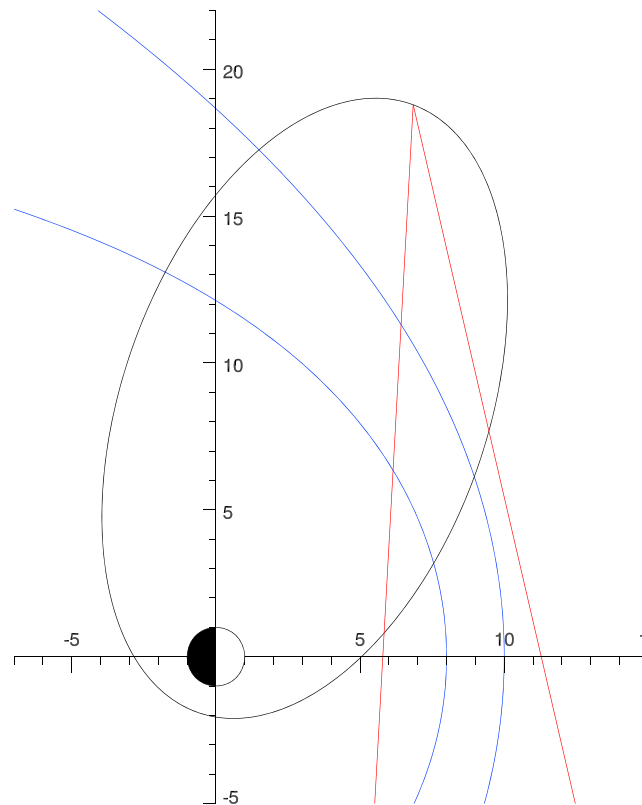
Figure 1. A sketch of the orbital and viewing geometry of the Solar wind Magnetosphere Ionosphere Link Explorer (SMILE) mission. The coordinate axes are in Earth radii. The horizontal axis points toward the Sun to the right of the plot, and the vertical axis is the Z axis, for example, in geocentric solar magnetospheric coordinates. The leftmost blue curve is the magnetopause, and the rightmost blue curve is the bow shock. The black ellipse is the orbit of the SMILE spacecraft, in this illustration as a 2×20 Earth radii orbit inclined 20° sunward. The red lines are separated by 16° illustrating the θ direction field of view of the SMILE Soft X-ray Imager camera.

and the MAGnetometer. Images of the magnetosheath will be provided by SXI, a soft X-ray telescope making use of the lobster-eye optic. SMILE will adopt a highly elliptical orbit with approximate parameters of an apogee of 19 R_E, a perigee of 1 R_E, and a period of 51 hr. The orbit will be highly inclined (67° or 98° depending on launch vehicle) to enable long exposures toward the northern auroral regions. Figure 1 illustrates the geometry of the problem. The black ellipse is a rough example of an orbit, in this case inclined somewhat toward the dayside. The blue curves are the magnetopause boundary and the bow shock boundary. The red lines are the FOV discussed in the next paragraph.

The latest design of the SXI has a FOV of 16° by 27° that is enabled using an X-ray mirror based on micropore optic technology in a lobster-eye configuration. Earlier designs of lobster-eye X-ray optics have been published by Collier et al. (2012) and by Peele et al. (2004). The charge-coupled device-based detector system provides spatial and energy resolution in the soft X-ray band. The detector array has 751 by 1,288 native pixels with a plate scale of approximately 1.2 arc min per charge-coupled device pixel; however, the point-spread function of the optic has a full-width half maximum of around 8 arc min. Sampling at this resolution gives an effective maximum array of around 120 by 200 superpixels.

Since the X-ray image of magnetosheath is absent in satellite observation currently, simulation of the SWCX emission is thus essential. Two-dimensional X-ray images have been simulated via integration of the emissions along lines of sight (LOSs), based on global magnetohydrodynamics (MHD) models (e.g., Sun et al., 2015; Robertson & Cravens, 2003; Robertson et al., 2006). These images give a preliminary hint of what the SXI on board SMILE may observe. To extract the 3-D magnetopause and bow shock shapes from these images, we propose a method of fitting a 3-D model of the emissions to the 2-D X-ray images.

In this paper we consider only the effects of photon noise. For that reason we must eliminate other sources of noise, including fitting error that results when the model being fit is not able to exactly reproduce the distribution behind the observations. For that reason we use the same model to generate the simulated images as we use for fitting those images to extract boundary parameters. In a separate paper we will explore the effects of fitting noise when the model is unable to exactly reproduce the distribution behind the simulated images. It is beyond the scope of this paper to consider the sensitivity of detection of boundaries as a function of exposure time, because this requires detailed knowledge of the SXI instrument simulator with all sources of instrumental background modeled as well as the source SWCX signal. The true signal to background ratio will vary based on instrument look direction, the characteristics of the local particle background, and, essentially, the strength of the solar wind. Exploration of the boundary detection method as described in this paper in this context will also be the subject of a further paper.

One other approach to boundary reconstruction should be mentioned. Collier and Connor (2018) use the tangent vector determined from so-called limb-brightening (Collier et al., 2014, 2005) to demonstrate the location of the magnetopause boundary from X-ray images.

Lastly, we should mention that imaging data such as these exist over a wide range of physical domains. For example, Energetic Neutral Atom images are often images of the ring current, a translucent object, and also contain boundaries, which can be detected. Extreme ultraviolet emissions from the scattering of sunlight by singly ionized helium in the Earth's plasmasphere is another example of a similar type of image, which contains boundaries. The techniques that are developed here for X-ray images can be equally well applied to these other types of images.

2. Simulated X-Ray Emissions

To simulate the SWCX X-ray emissions, we first run the global MHD code to get the plasma density, bulk velocity, and thermal speed in the magnetosheath and then use these parameters to estimate the emission rate.

2.1. MHD Model

The PPM (piecewise parabolic method)-MHD code was used to simulated the solar wind-magnetosphere-ionosphere system. It was developed by Hu et al. (2007) and employs an extended Lagrangian version of the piecewise parabolic method to solve the MHD equations in the solution domain: $-300\,R_E \leq x \leq 30\,R_E$, $-150\,R_E \leq y, z \leq 150\,R_E$. The minimum grid spacing is $0.1\,R_E$. The ionosphere, simplified as a spherical shell, is assumed to have a uniform Pedersen conductance (5 S in this paper) and a zero Hall conductance. It is coupled with the inner boundary of the magnetosphere, which is set to be a spherical shell at $r = 3R_E$. The effect of the Earth's dipole tilt was not considered in this study.

The solar wind conditions adopted in this simulation run are as follows: solar wind density $N = 22.5$ cm^{-3}; velocity $v_x = 400$ km/s, $v_y = v_z = 0$; and interplanetary magnetic field $B_x = B_y = 0$, $B_z = 5$ nT. The MHD simulation is mainly used to arrive at the functional forms of magnetopause/bow shock positions and the X-ray emissivity (i.e., equations (7) and 8 as follows). We have tested with another MHD simulation run under average solar wind flux. It is found that the present functional forms apply well for both MHD runs.

2.2. Emissions Simulation

The volume emission rate is then estimated by (Cravens, 2000):

$$P = \alpha_{cx} n_H n_{sw} \langle g \rangle \quad (eV \cdot cm^{-3} \cdot s^{-1}), \tag{1}$$

where α_{cx} is an efficiency factor dependent on the SWCX cross section, compositions, and abundances of the solar wind heavy ions and so on. As α_{cx} ranges from 6×10^{-16} to 6×10^{-15} eV cm^2 according to Cravens (2000), we adopt $\alpha_{cx} = 1.0 \times 10^{-15}$ eV cm^2 in this paper. Number densities of plasma and the exospheric hydrogen are denoted by n_{sw} and n_H, respectively. The value of n_{sw} is provided by the MHD simulation, and a reasonable approximation of n_H is chosen: $n_H = 25\,(\text{cm}^{-3})(10(R_E)/r)^3$ (Cravens et al., 2001; Hodges, 1994). $\langle g \rangle = \sqrt{u_{sw}^2 + u_{th}^2}$, which is the average collision speed estimated by the plasma bulk speed u_{sw} and thermal speed u_{th}.

The X-ray intensity along a specific LOS is obtained by line integration of P:

$$I = \frac{1}{4\pi} \int P dr \quad (keV \cdot cm^{-2} \cdot s^{-1} \cdot sr^{-1}), \tag{2}$$
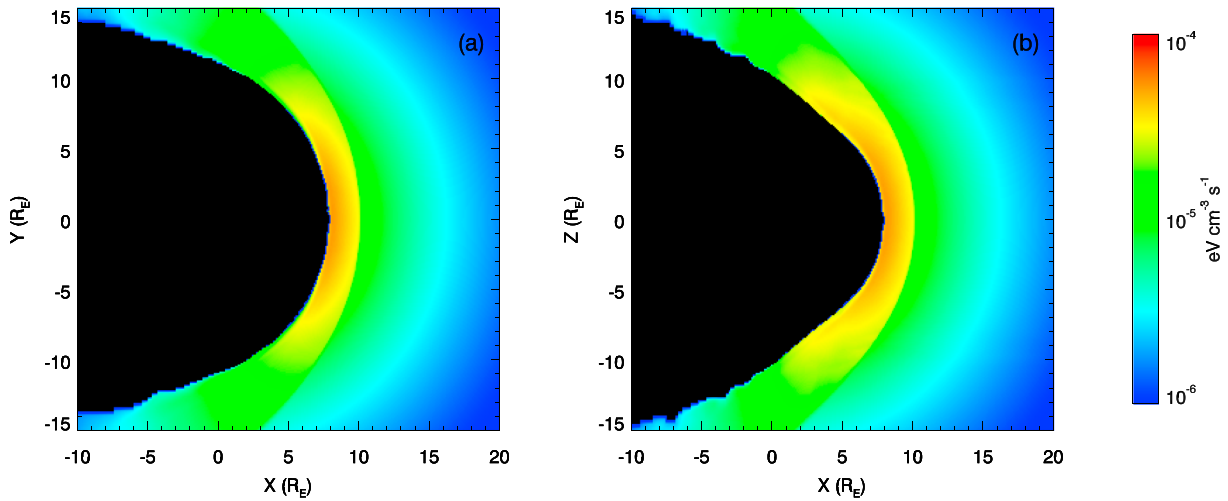
Figure 2. Section in the (a) $z = 0$ plane and (b) the $y = 0$ plane of X-ray emissions computed from the magnetohydrodynamics model.

This integration starts from the observation point to $r = 80 R_E$, beyond which the geocoronal SWCX emission is neglected due to the sparse exospheric hydrogen there. There is of course an astronomical background of X-ray emissions. Later in this paper we consider a simple model for the astronomical background. In observations the real astronomical background, derived from astronomical observations (e.g., Snowden et al., 1995), needs to be considered. An important part of this calculation is the identification of the magnetopause, because it is assumed that inside the magnetopause, where the density of high charge state ions is much lower, the X-ray emission is negligible. We use the flux method to locate the magnetopause position in the MHD result. More specifically, from the magnetosheath to the magnetosphere, the plasma flux sharply decreases at the magnetopause. First, the transition region is found, and then inside this region, we define the places where the plasma flux decrease to half of the solar wind level as the magnetopause position. This method returns a relatively smooth magnetopause (see Figure 4), except for the region close to the subsolar point where the plasma velocity and the flux decrease to 0. We then analyze the gradients of number density and thermal pressure, current density variation, and magnetic field direction together to identify the magnetopause at the subsolar point. Afterward, the X-ray emission rate is set to be 0 inside the magnetopause, as shown in Figure 2.

2.3. Image Simulation

The camera is assumed to be a rectangular pixel array with the individual pixel look directions assumed to be in an angular rectangular arrangement around the central axis of the camera.

The camera coordinate system is such that the look direction of the camera is along the positive X axis, $(\pi/2, 0)$ in standard spherical coordinates. The camera has N pixels in the vertical, Z, direction, and M pixels in the horizontal, Y, direction. FOV Θ is in the vertical direction and Φ in the horizontal direction. Each pixel then has an angular width of $\Delta\theta = \Theta/N$ in the vertical direction and $\Delta\phi = \Phi/M$ in the horizontal direction. The pixel numbering is from 0 to $N-1$ in the vertical direction and from 0 to $M-1$ in the horizontal direction. The center of pixel (i, j) looks in the direction

$$\begin{pmatrix} \theta \\ \phi \end{pmatrix} = \begin{pmatrix} \frac{\pi}{2} - \frac{\Theta}{2} + \Delta\theta\left(i + \frac{1}{2}\right) \\ -\frac{\Phi}{2} + \Delta\phi\left(j + \frac{1}{2}\right) \end{pmatrix} \tag{3}$$

Once the camera is rotated from the spacecraft coordinate system to the magnetospheric coordinate system, the geometry looks similar to Figure 1 in which the θ direction FOV is illustrated by the two red lines separated by an angle $\Theta = 16°$. The ϕ direction is in and out of the page in this view.

The value in each pixel is obtained by evaluating the integral equation (2). We use Gauss-Kronrod integration (Kronrod, 1965) for the LOS integral, because it is one of the most computationally efficient implementations of Gaussian quadrature integration. The efficiency is a result of the computation reusing function evaluations as intervals are subdivided. When pixels are large, it is necessary to do multiple LOS integrals
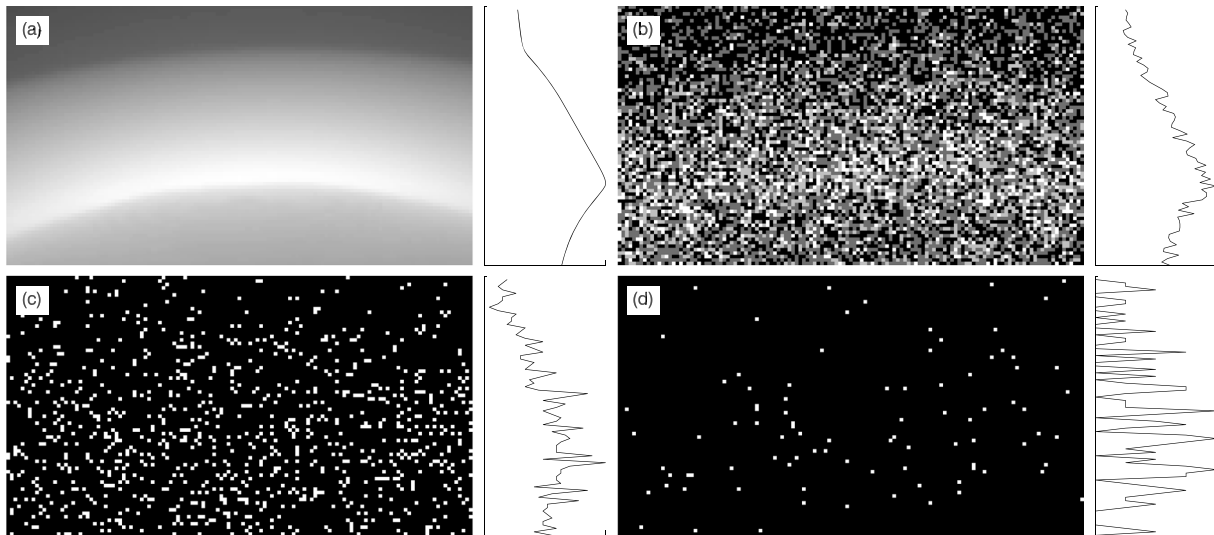
Figure 3. Simulated images of X-ray emissions from the magnetohydrodynamics model using the camera geometry in section 2.3 with dimensions 75 by 129 pixels and X-ray emissions from section 2.2. (a) Noise-free image, (b) image with 1 photon per pixel, (c) 0.1 photons per pixel, and (d) 0.01 photons per pixel, assuming Poisson statistics. To the right of each image is plotted the horizontal integral to guide the eye in recognizing the boundaries.

inside the pixel, at noninteger pixel coordinates between $i - \frac{1}{2}$ and $i + \frac{1}{2}$, and $j - \frac{1}{2}$ and $j + \frac{1}{2}$. However, for the present work the pixels are small enough that a single LOS integral suffices to represent the pixel value.

In this paper we assume a camera of 75 by 129 pixels, in other words 100 times fewer pixels than the images which are expected from the SXI camera on SMILE. This is done in order to reduce the computational burden for this paper as a very large number of images are simulated and fitted.

Figure 3a shows a simulated noise-free image, whereas Figures 3b–3d show the same image with average pixel count rates of 1, 0.1, and 0.01 counts, assuming Poisson statistics.

The boundaries can be clearly discerned in the noise-free image as well as in the higher count rate images and less well in the lowest count rate image. However, even at 0.01 photons per pixel average the boundaries may be discernible by eye. Because this is a two-dimensional project ion of the three-dimensional boundaries, some processing and assumptions are required in order to extract the boundary geometries.

3. Model

In order to determine the boundary locations, we fit an emissions model that consists of parametric descriptions of the locations of boundaries and parametric expressions for the brightness distribution between the boundaries.

3.1. Boundary Model

Figure 4a shows the magnetopause boundary (black) in the YZ plane for several different values of $\theta = 10°$, $20°$, $40°$, $80°$, and $120°$; Figure 4b shows the bow shock (black) in the YZ plane for $\theta = 10°$, $20°$, $40°$, $70°$, and $100°$. The θ coordinate of a point is the angle between the vector to that point and the x axis of the coordinate system, which points in the direction of the sun. A particular value of θ does not correspond to a fixed value of x for the whole ellipse, but in this case in Figures 4a and 4b, the corresponding x coordinates for each ellipse are similar. The green ellipses are least-absolute-deviation fits of radius of the model:

$$\begin{pmatrix} y \\ z \end{pmatrix} = \begin{pmatrix} r_y \cos \phi + y_o \\ r_z \sin \phi + z_o \end{pmatrix} \tag{4}$$

where ϕ is the angle around the x axis in the right-hand sense starting at the y axis. Figures 4a and 4b demonstrate that the ellipse is an excellent fit to both the magnetopause and bow shock at a fixed value of θ, except perhaps at $\theta = 120°$ for the bow shock in Figure 4b, which is not observed in the images. We also found that y_o and z_o are negligibly small, $< 0.1\ R_E$, so we ignore them in the following.
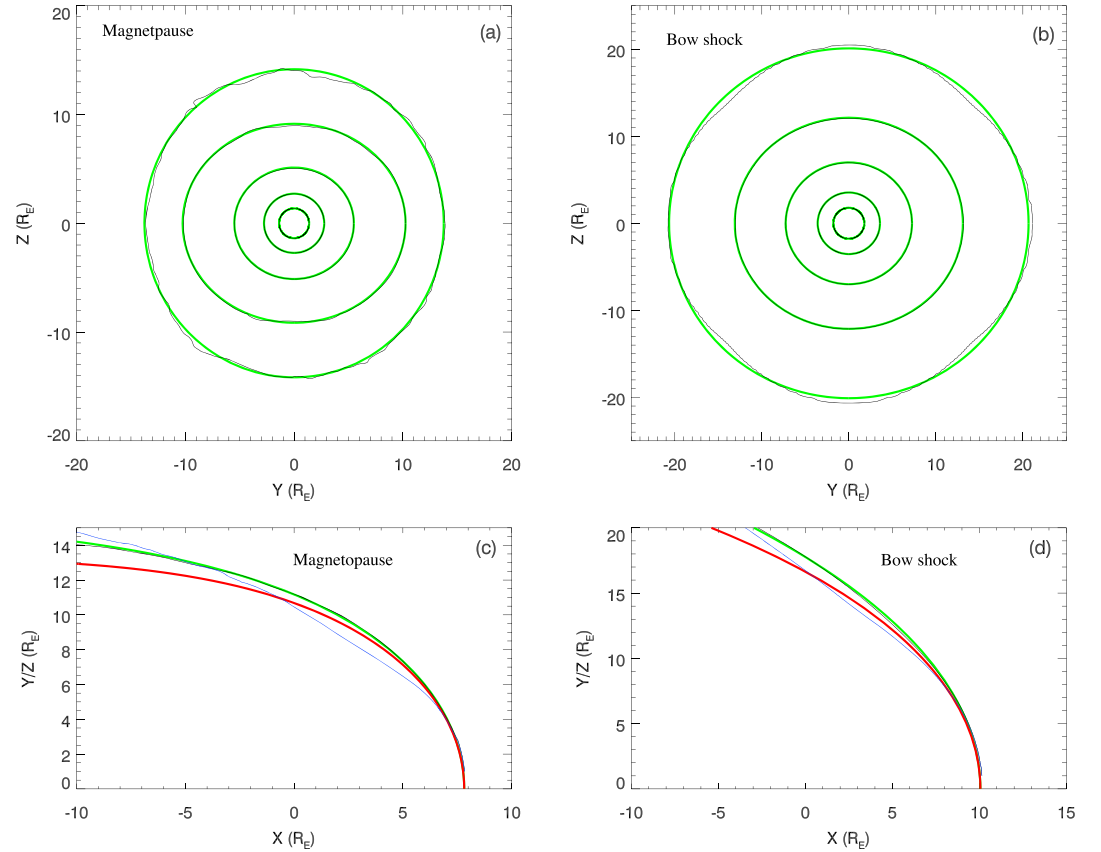
Figure 4. Fitting the model to the boundaries derived from the magnetohydrodynamics model. (a and c) Fits to the magnetopause and (b and d) fits to the bow shock. In panel (a) the black curves plot the distance of the magnetopause from the x axis for fixed values of $\theta = 10°$, $20°$, $40°$, $80°$, and $120°$ (innermost to outermost), whereas the green ellipses are the best fit. In panel (b) the black curves plot the distance of the bow shock from the x axis for fixed values of $\theta = 10°$, $20°$, $40°$, $70°$, and $100°$ (innermost to outermost), whereas the green ellipses are the fit. In panel (c) the black curve is r_y obtained from ellipse fits, the green curve is the cross section of the fitted magnetopause, the blue curve is r_z, and the red is the corresponding cross section of the fitted magnetopause. Panel (d) shows the same quantities as panel (c) but for the bow shock.

Figures 4c and 4d show r_y and r_z as a function of x coordinate (in this case $x = r \cos \theta$), the magnetopause in Figure 4c and the bow shock in Figure 4d. The curve for r_y is plotted in black, r_z in blue. To those two curves we fit the Shue et al. (1997) model, for $x > -5 R_E$:

$$r_y(\theta) = r_0 \left(\frac{2}{1 + \cos \theta} \right)^{\alpha_y} \tag{5}$$

and

$$r_z(\theta) = r_0 \left(\frac{2}{1 + \cos \theta} \right)^{\alpha_z} \tag{6}$$

with the same value r_0 for the two models. The green curves is the fit to r_y, and the red curve is the fit to r_z. The Shue et al. (1997) model is an excellent fit to r_y and a somewhat less good fit to r_z. Nevertheless, we decide to use this model as a reasonable approximation of the shape of the magnetopause and of the bow shock in the following work. In this way we have produced a three-dimensional generalization of the Shue et al. (1997) model:

$$r(\theta, \phi) = \frac{r_y(\theta) r_z(\theta)}{\sqrt{\left[r_z(\theta) \cos \phi \right]^2 + \left[r_y(\theta) \sin \phi \right]^2}} \tag{7}$$

where θ is the angle from the X axis and ϕ is the rotation angle in the right-hand direction around the X axis starting at the Y axis.
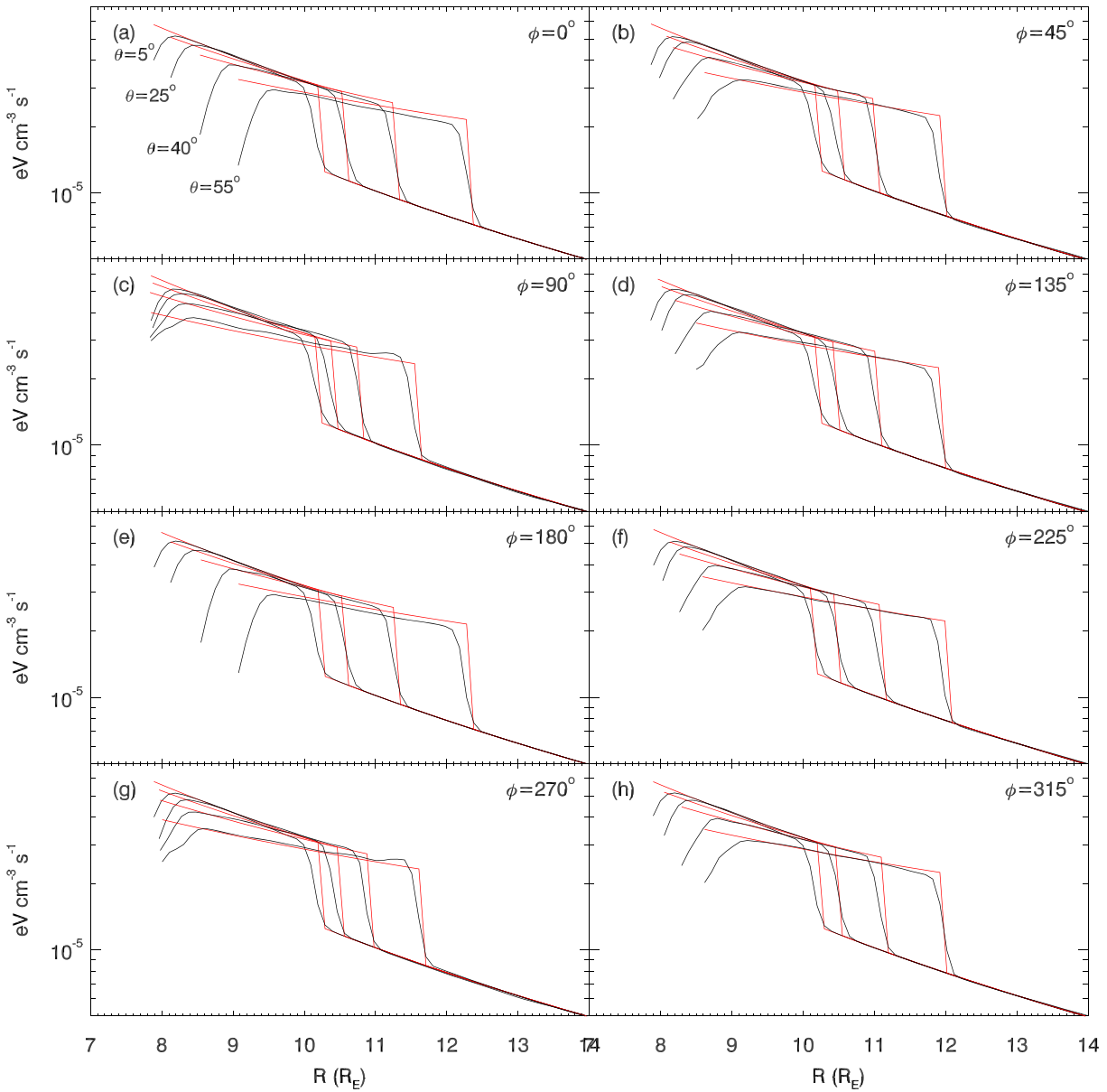
Figure 5. Profiles of brightness derived from the magnetohydrodynamics model (black curves) and from a best fit model of equation (8) (red curves). The parameters of the best fit model are $A_1 = 3.23 \times 10^{-5}$ eV·cm^{-3}·s^{-1}, $B = -9.4 \times 10^{-6}$ eV·cm^{-3}·s^{-1}, $\alpha = 2.38$, $\beta = -1.23$, $A_2 = 1.36 \times 10^{-5}$ eV·cm^{-3}·s^{-1}.

3.2. Emissions Model

Between the boundaries and in the solar wind we use an emissions model which is intended to have a similar shape to the emissions computed from the MHD model, the emissions shown in Figure 2. We arrived at the following model through some experimentation, plotting observations and some educated guesses at functional forms, which would approximately represent the emissions. The function we eventually settled on is by no means the last word but merely represents a function which appeared good enough. The function is

$$
F\left(\vec{r}\right) = \begin{cases} 0 & \text{inside MP} \\ \left(A_1 + B\sin^8\theta\right)\left(\dfrac{r}{r_{\text{ref}}}\right)^{-\left(\alpha+\beta\sin^2\theta\right)} & \text{between MP and BS} \\ A_2\left(\dfrac{r}{r_{\text{ref}}}\right)^{-3} & \text{outside BS} \end{cases} \tag{8}
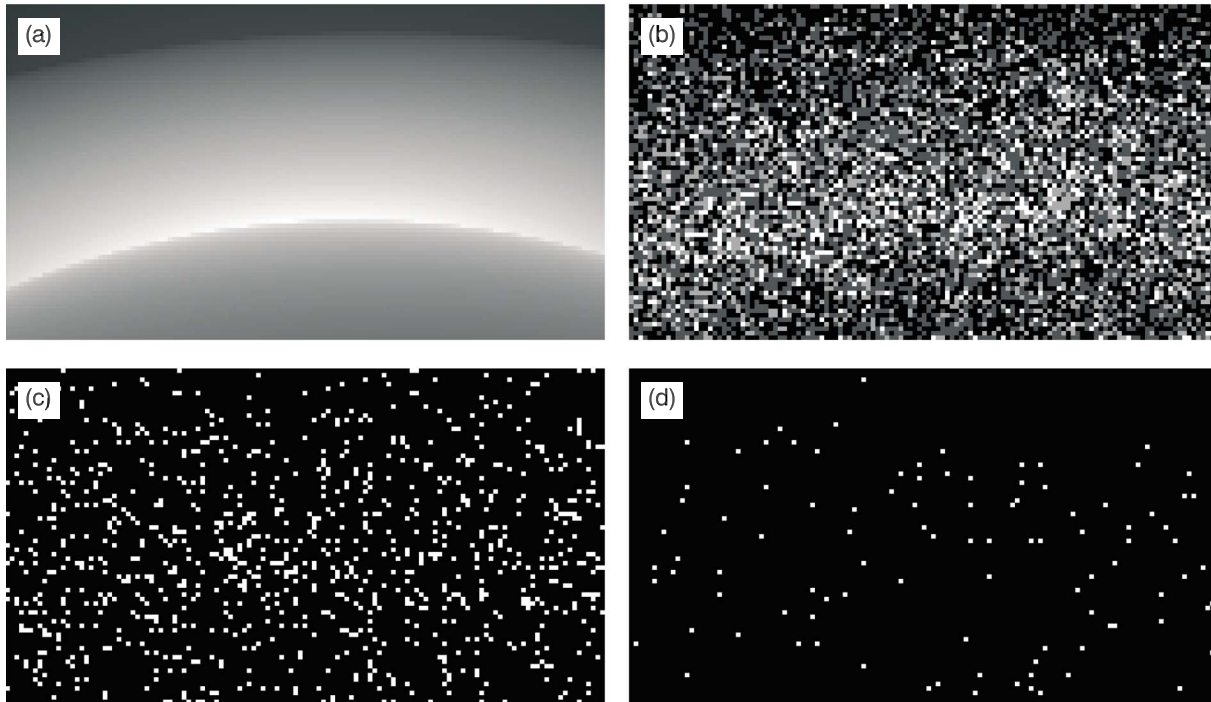$$

Figure 6. Simulated images of X-ray emissions using the camera geometry in section 2.3 with dimensions 75 by 129 pixels and X-ray emissions from the analytical model. (a) Noise-free image, (b) image with 1 photon per pixel, (c) 0.1 photons per pixel, and (d) 0.01 photons per pixel, assuming Poisson statistics.

where $r_{\text{ref}} = 10\,R_E$ is a constant. Figure 5 shows radial profiles of the emissions from the MHD model (black curves) together with a best fit model equation (8) (red curves). The best fit of model is found by minimizing the absolute difference between the mathematical model and the MHD model.

Figure 6 shows images in the same format as Figure 3 for the model developed above. We used the following parameters for equation (8)$A_1 = 3.2285 \times 10^{-5}$ eV·cm^{-3}·s^{-1}, $B = -1.7985 \times 10^{-5}$ eV·cm^{-3}·s^{-1}, $\alpha = 2.4908$, $\beta = -1.6458$, $A_2 = 1.3588 \times 10^{-5}$ eV·cm^{-3}·s^{-1}, and parameters $r_0^{\text{mp}} = 8\,R_E$, $\alpha_y^{\text{mp}} = 0.5805$, and $\alpha_z^{\text{mp}} = 0.4082$ for the magnetopause, and $r_0^{\text{bs}} = 10\,R_E$, $\alpha_y^{\text{bs}} = 0.7827$, and $\alpha_z^{\text{bs}} = 0.7979$ for the bow shock. These parameters are obtained by a fit, and comparing the images in Figure 6 with those in Figure 3 suggests that this is a close fit for the region imaged. We should point out that the number of significant digits does not mean that the analytical model fits the MHD-derived X-ray emissions to this level of accuracy: It does not. If we chose a different set of points to fit to, we would have obtained a different set of parameters. These values came out of one fit, and we decided to use them as is, and it is important that we use the same values as inputs to the model, which makes the images as we use for the initial guess when fitting. By changing the points to which we fit, we can certainly obtain different values by many percent, for some parameters tens of percent.

The following images are generated using this set of parameters in the analytical model, and the analytical model is fit to the images, using these same parameters as initial guesses, to extract the parameters.

4. Fitting Approach

To obtain the location and shape of the magnetopause and bow shock from an image, we generate simulated images using the procedure in section 2.3 of the emissions in equation (8) with the magnetopause and bow shock defined by equation (7). We vary the parameters of that model until we have an optimal match between the modeled image and the MHD model simulated image. The list of parameters that are varied is A_1, B, α, β, A_2, r_0^{mp}, α_y^{mp}, α_z^{mp}, r_0^{bs}, α_y^{bs}, and α_z^{bs}.

As the minimization algorithm we used the Nelder and Mead simplex method (Nelder & Mead, 1965), which minimizes a cost function. We wish to maximize the probability of the Poisson image given the fitted image

$$p = \prod_i^N \prod_j^M p(c_{ij}; a_{ij}) \tag{9}$$

where i, j count the pixels, c_{ij} are the pixel counts in the image to be fitted, a_{ij} is the expectation value of the pixel count in the fitting image, and $p()$ is the Poisson probability function. p is a very small number, and the optimization algorithm requires minimization so we will instead minimize the negative of the sum of the logarithms of probabilities:

$$f_{\min} = -\sum_{i=1}^{N}\sum_{j=1}^{M} \log_{10}\left[p(c_{ij}; a_{ij})\right] \qquad (10)$$

With these tools we were able to carry out several different experiments to determine how well a three-dimensional boundary can be extracted from two-dimensional noisy images.

5. Results

To test the approach of fitting a 3-D analytical function to 2-D noisy images, we carry out four separate experiments. In section 5.1 we examine how the accuracy of the reconstruction depends on the photon counts. In section 5.2 we examine how the accuracy and biases depend on the orbital position of the spacecraft and the changing viewing geometry. In section 5.3 we examine how the accuracy depends on the viewing direction of the camera. In section 5.4 we examine how the accuracy depends on the presence of a background in the images. The fitting algorithm test about the global minimum is shown in section 5.5.

5.1. Signal-to-Noise Ratio Dependence

To investigate the dependence of parameters and their uncertainties on the number of counted photons in an image, we selected a single satellite position and a look direction. For that configuration we generate an image, the image in Figure 6a. Then we generate ensembles of images for different average count rates, including Poisson noise. We generated 100 images at each of 13 logarithmically spaced counts between 0.005 and 16 counts per pixel. From those results we can compute the mean and standard deviation of the parameters. Figure 7 plots the mean and standard deviation of the magnetopause parameters as a function of the number of counts per pixel. Figures 7a and 7c are for the magnetopause, while Figures 7b and 7d for the bow shock. Figures 7a and 7b plot the average of parameters r_0, α_y, and α_z, while Figures 7c and 7d plot their standard deviations. In the left column are parameters for the magnetopause and in the right column the parameters for the bow shock. The black curves are for r_0, the red curves for α_y, and the blue curves for α_z.

We first notice that in Figures 7a and 7b the curves appear to be independent of count rate. This means that count rate variation does not introduce a bias in the measurements. This is as we expect. We also notice that the uncertainty on parameters varies approximately as the number of counts per pixel to the negative one-half power, except for σ_y at the bow shock. This variation of uncertainty with the count rate to the negative one-half power is as expected from theory when extracting information from counting data. The bow shock σ_y variation is not as steep: In fact, its variation appears to be closer to the negative one-fourth power. This may be due to the fact that σ_y is already not as well determined and thus the uncertainty may effectively saturate. Another possibility (proposed by one of the reviewers) is that at lower count rate the uncertainty in α_y is absorbed by another parameter due to degeneracy between the parameters.

We see that to achieve an uncertainty of $0.1\,R_E$ in the determination of the distance to the subsolar point on the magnetopause approximately 0.1 counts per pixel is required, corresponding to $129 \times 75 \times 0.1 \approx 10^3$ counts in the image. For the bow shock approximately half the number of photons are required.

The curvature of the magnetopause and bow shock are determined by the value of α_y and α_z separately for each. The value α_y is the curvature in the dawn-dusk direction and thus is approximately the curvature across the image plane, whereas α_z is the curvature in the noon-midnight plane, approximately perpendicular to the image plane. Comparing Figure 7c and Figure 7d we notice that α_z has smaller uncertainty than α_y for the same count rate. For example, at 0.1 counts per pixel the uncertainty on α_y is 0.3, whereas the uncertainty on α_z is 0.2. For the bow shock the uncertainties are 0.25 and 0.07 for α_y and α_z, respectively.

A possible explanation for the smaller uncertainty in the direction perpendicular to the image plane is that the camera is imaging a larger section of the magnetopause and bow shock in that direction. The boundary extends a large distance toward and away from the camera before it curves out of the image in that direction. In the direction parallel to the image plane, by contrast, only a much smaller portion of the boundary is
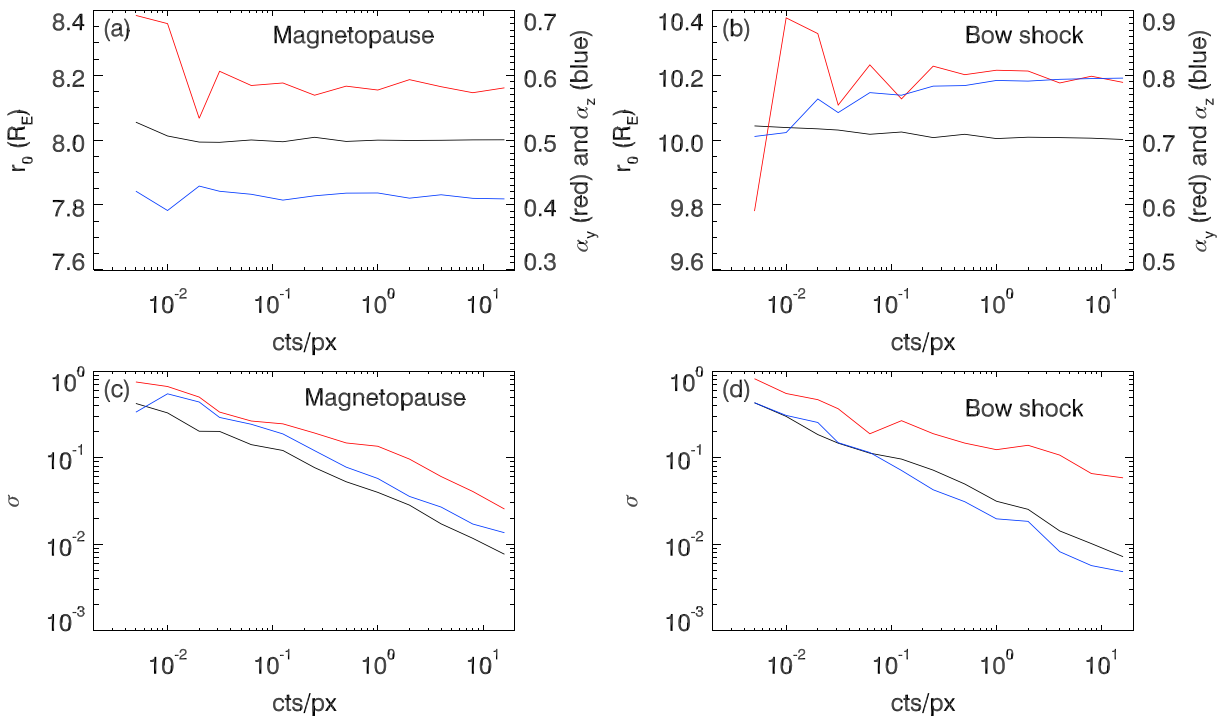
Figure 7. Reconstruction results as a function of average photon count rate per pixel. (a and c) The magnetopause and (b and d) the bow shock. Panels (a) and (b) show the average values, while panels (c) and (d) show the standard deviations. In all panels the black curve is for r_0, the red curve for α_y, and the blue curve for α_z.

imaged. This can be better understood by referring to the sketch in Figure 1. The length of either boundary covered in the y direction in the equatorial plane cannot be greater than about $9\,R_E$, which is the distance subtended by the 27° FOV at a range of $20\,R_E$. By contrast in Figure 1 it appears that about $15\,R_E$ of magnetopause is covered in the z direction and perhaps $25\,R_E$ of bow shock. This may explain why the shapes are better constrained in the z direction. However, this result relies on the brightness image and the model being very close matches to each other to avoid fitting errors.

Given the relatively large fractional uncertainties on α_y and α_z, it is important to determine how this affects uncertainty on the position of the boundaries away from the subsolar point. Because while at the subsolar point the uncertainties on the boundary position are exactly the uncertainty on r_0, away from the subsolar point it is a combination of the uncertainty on r_0 and on α. We use the parameters for each ensemble image to compute a magnetopause and bow shock shape, using equation (7). This then gives us an ensemble of boundary distances from the Earth in all direction from which we can compute standard deviations. Figure 8 shows the results of this, plotting the uncertainty on the distance to the magnetopause and bow shock as a function of angle θ from the subsolar point, in the XY plane (top row) and the XZ plane (bottom row).

The inflection point in the curves in Figure 8 is probably related to where the boundary exits the image, although it should be kept in mind that the boundary leaves the image at different values of θ in the Northern and Southern Hemispheres (see Figure 1) as well as at the dawnside and duskside of the image. Naturally, the uncertainty will be the same at $\theta = 0°$ along the Y axis and the Z axis, because it is the same point. Moving away from $\theta = 0°$, we see that the uncertainty either decreases or remains low for larger angles or both for the Z axis compared with the Y axis. That is consistent with the smaller values for the uncertainty of α_z obtained in Figure 7. In some cases the uncertainty (the ensemble standard deviation) on the boundary distance is a little smaller away from the subsolar point than it is at the subsolar point.

5.2. Orbital Position Viewing Geometry Dependence
It is most desirable if the determination of the boundaries is independent of (i.e., not biased by) the location of the spacecraft in its orbit. To investigate how the parameters depend on orbital position of the spacecraft, we generated images corresponding to an apogee pass in the SMILE nominal orbit.
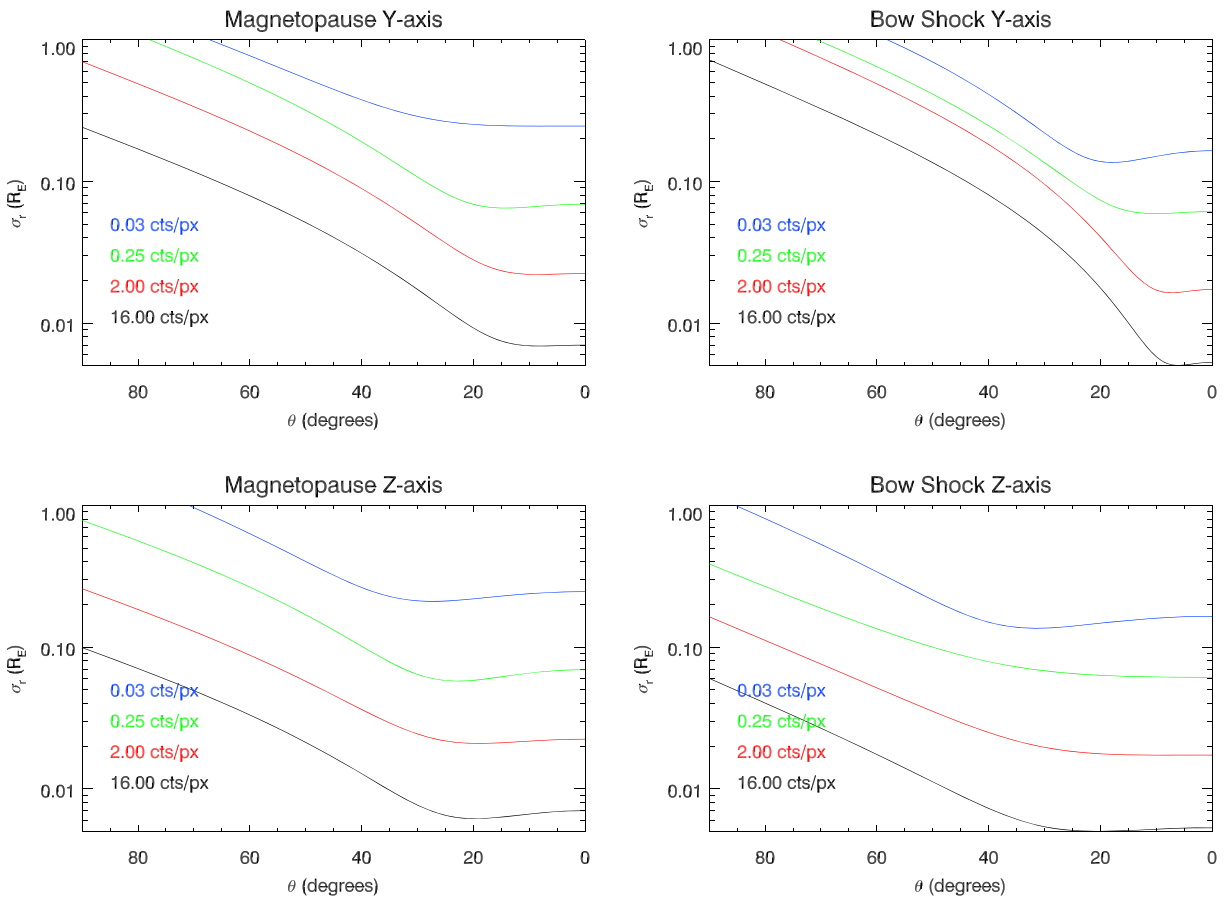
Figure 8. Uncertainty in the location of the magnetopause as a function of angle θ from the subsolar point for representative pixel counts. Uncertainty along (a) the Y axis for the magnetopause, (b) the Y axis for the bow shock, (c) the Z axis for the magnetopause, and (d) the Z axis for the bow shock.
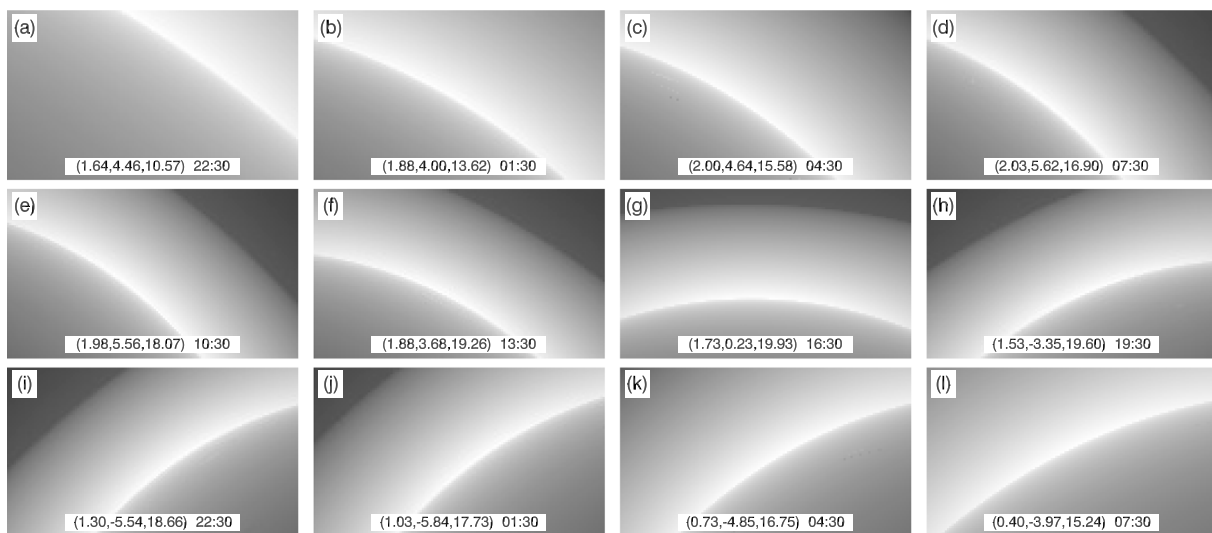

Figure 9. Sequence of images for one apogee pass. The inset text in each image is the spacecraft position in Earth radii in the geocentric solar magnetospheric coordinate system and the universal time of the image. The time from the first image, (a), to the last image, (l), is 36 hr. The center of each image points at the geocentric solar magnetospheric location $(x, y, z) = (9.5, 0, 0) R_E$.
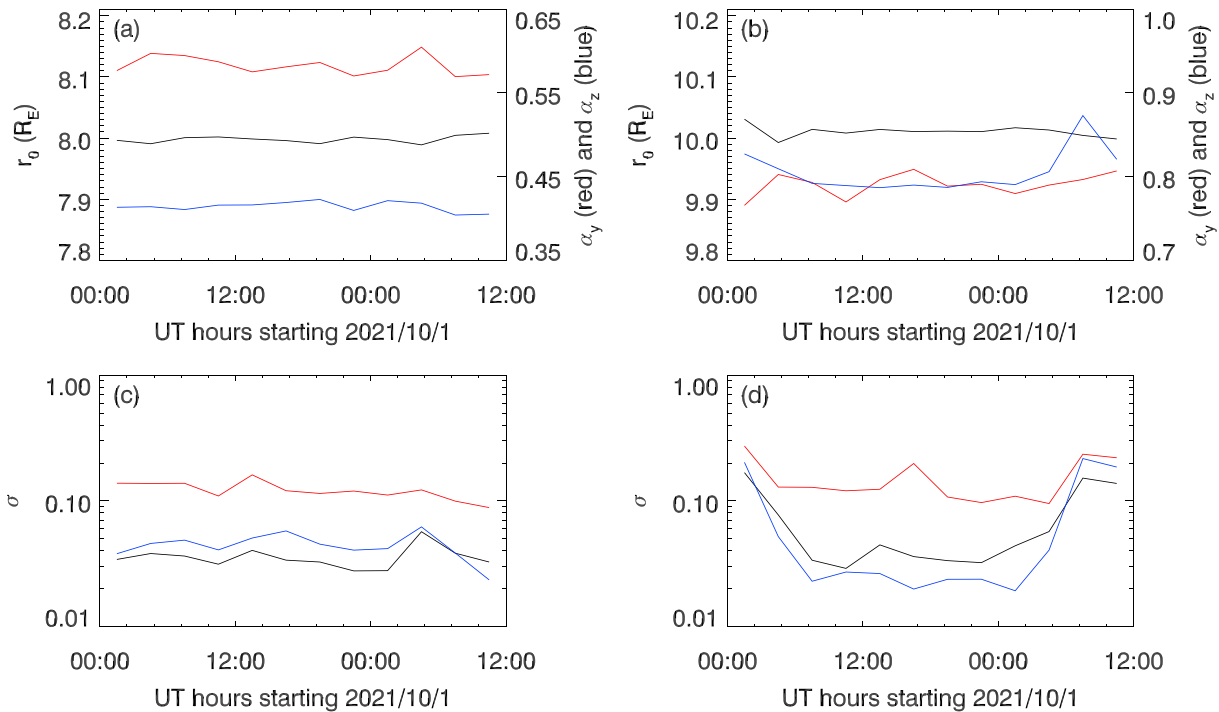
Figure 10. The fitting parameters and their uncertainties for the magnetopause (a, c) and the bow shock (b, d). The top row are the average values, and the bottom row the standard deviations. In all panels the black curve is for r_0, the red curve is for α_y, and the blue curve for α_z. In the top row the black curve is referenced to the left-hand Y axis, while the red and blue curves are referenced to the right-hand axis. In the bottom row the standard deviation of r_0 is in R_E.

Figure 9 shows the images, without noise, and the inset text shows the location of the spacecraft in Earth radii in the geocentric solar magnetospheric coordinate system (e.g., Russell, 1971) as well as the time of the image. In all images the camera points at the location $(x, y, z) = (9.5, 0, 0)\,R_E$ and the camera orientation is such that the x axis of the image is parallel to the geocentric solar magnetospheric xy plane. We can see that in both the first and last image there is almost no clear view of the bow shock boundary in the images. The length of the section of the magnetopause which is visible also is a function of the orbital position. The time from the first image, (a), to the last image (l), is 33 hr, and the images are separated by 3 hr.

We added noise corresponding to an average of 1 count per pixel in each image and fitted the emission distribution function and boundary locations to that using a Monte Carlo sample of 100 at each time. Figure 10 shows the results of the fits. Figures 10a and 10c are for the magnetopause, whereas Figures 10b and 10d are for the bow shock. The first row is average values of the fitted parameters, and the second row the standard deviation. In all panels the black curve is for r_0, the red curve for α_y, and the blue curve for α_z. We see that for the most part the curves in the top panel are horizontal, which means that the retrieved parameters are not dependent on the orbital position and thus viewing geometry of the spacecraft. The possible upward curvature of the blue curve in Figure 10b (α_z^{bs}) is consistent with noise fluctuations and not indicative of a bias. In the bottom row there is very little change in the standard deviation of the retrieved parameters for the magnetopause, in Figure 10c. For the bow shock there is a signature of the orbital position and viewing geometry. At the ends of the interval the uncertainty of the retrieved parameters are significantly larger. In the case of r_0 the uncertainty at the ends of the interval is as much as 5 times larger, for α_y twice as large, and for α_z 10 times as large. If we examine Figure 9, we see a reason for this; at the extreme ends of the interval there is only a very limited view of the bow shock.

5.3. Viewing Direction Dependence

To determine the dependence of reconstruction on the viewing direction, and how large a portion of each boundary is visible, we carried out the following experiment. We use the same vantage point and image rotation as in section 5.1, but the target location is varied from $5\,R_E$ to $13\,R_E$ along the positive X axis in steps of $0.5\,R_E$. In section 5.1 the target is located $9.5\,R_E$ along the positive X axis. Figure 11 shows several representative images, including the closest (Figure 11a) in and furthest out (Figure 11d) image. In Figure 11a
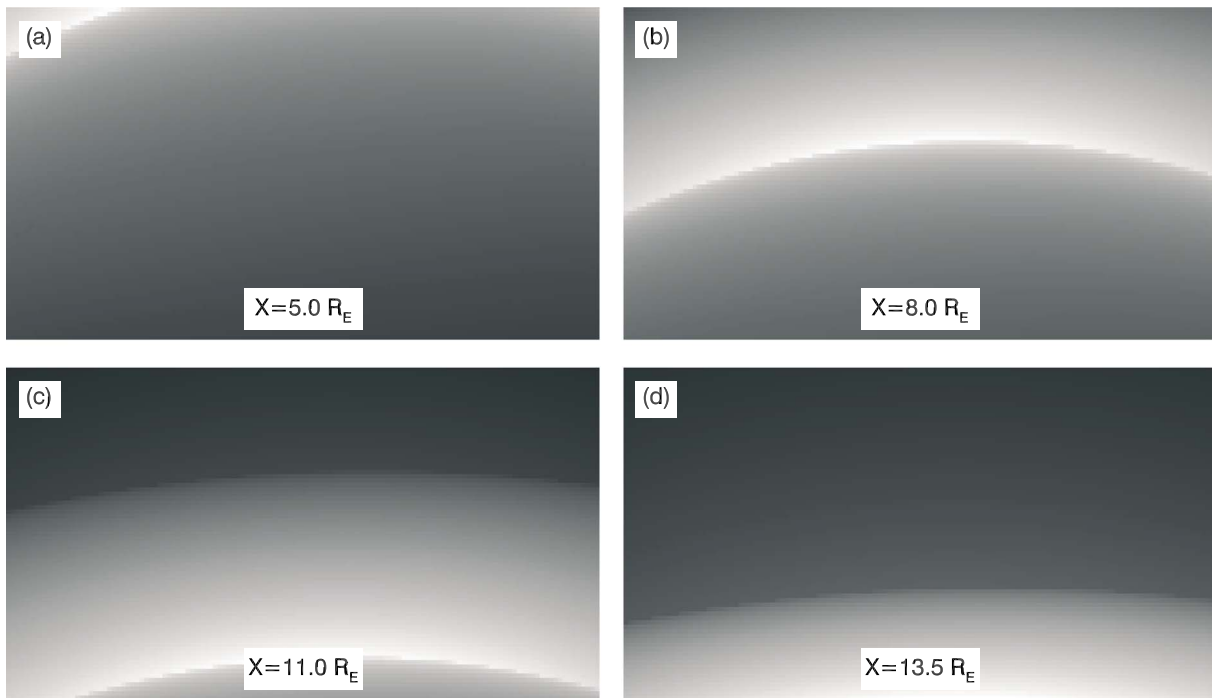
Figure 11. Images generated from the same vantage points as in Figure 6 but with different viewing directions. (a) Looking at target location $(5.0, 0, 0)\, R_E$, (b) at target location $(8.0, 0, 0)\, R_E$, (c) $(11.0, 0, 0)\, R_E$, and (d) at $(13.5, 0, 0)\, R_E$.
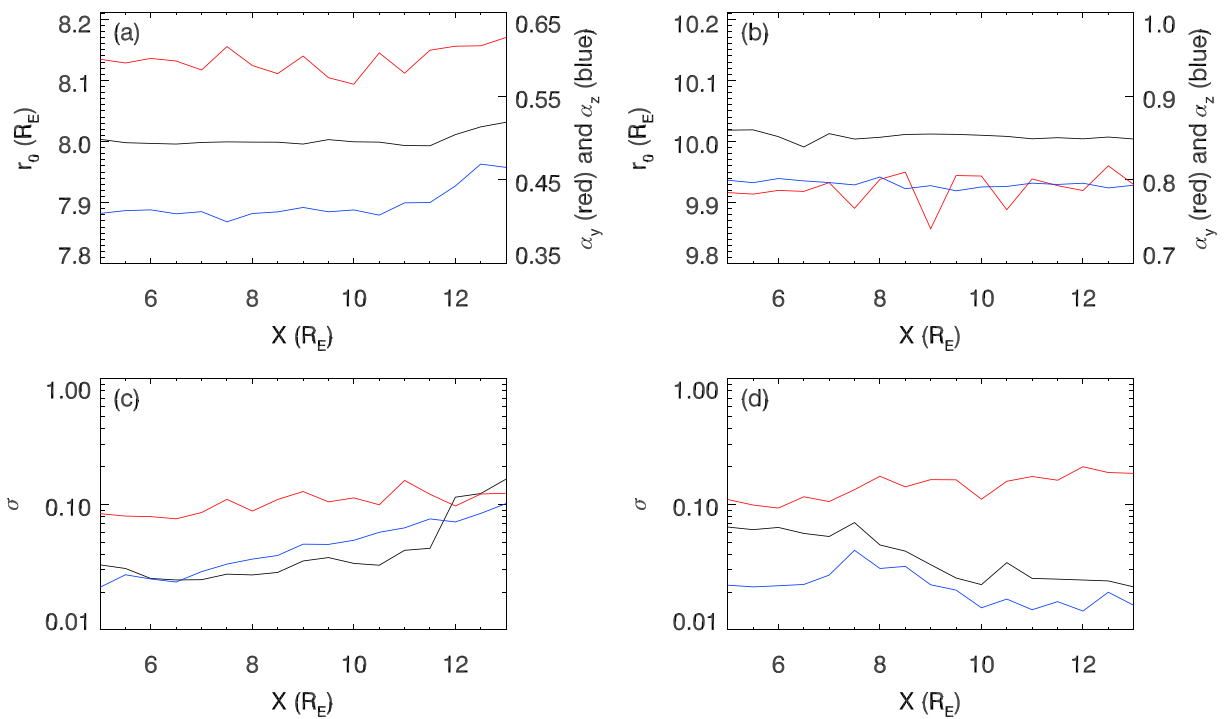

Figure 12. Plot of position reconstructed parameters of the magnetopause and bow shock as a function of the target location X coordinate. (a and c) The magnetopause and (b and d) the bow shock. The top row plots average parameters, and the bottom row the standard deviation. The black curves are for r_0, the red curves for α_y, and the blue curves for α_z.
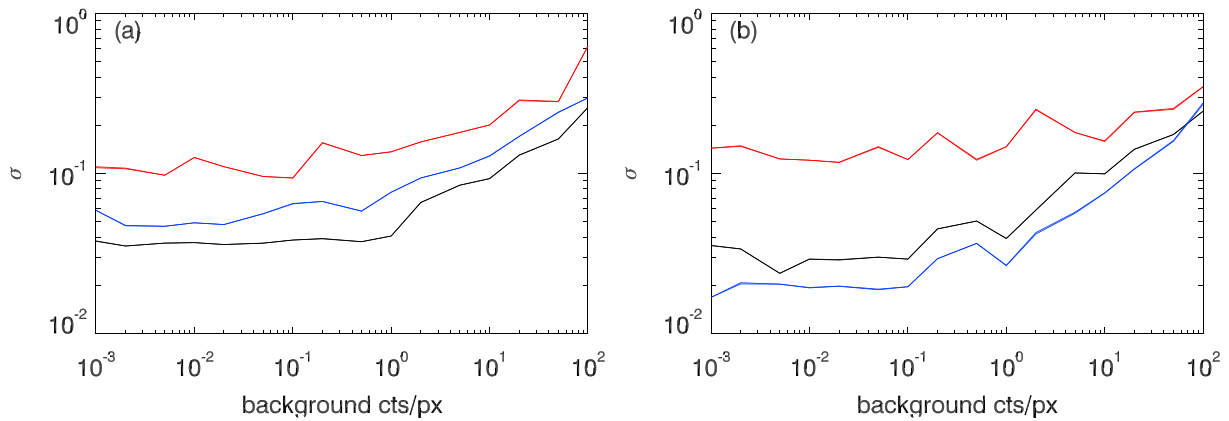
Figure 13. Uncertainty of reconstructed(a) magnetopause and (b) bow shock parameters as a function of a known background magnitude. In each panel the black curve is the standard deviation of r_0 in R_E, the red curve the uncertainty on α_y, and the blue curve the uncertainty on α_z.

the bow shock boundary is not visible in the image, and the magnetopause boundary is only visible in the upper left corner of the image, while in Figure 11d the magnetopause boundary is not visible.

Figure 12 plots the dependence of the average value as well as standard deviation of the magnetopause and bow shock parameters. In Figures 12a and 12b are the average values, and in Figures 12c and 12d are the standard deviations. In the left column are the parameters for the magnetopause, while in the right column are the parameters of the bow shock. In each panel the black curve is for r_0, the red curve for α_y, and the blue curve for α_z. Looking first at the magnetopause the reconstructed parameters are constant for all values of X smaller than about 11 R_E. At that point an increase in r_0, α_y, and α_z is observed, and looking at Figure 11 it is the point at which the magnetopause boundary disappears from the image. At that point the uncertainty in r_0 increases sharply, as well as there are fewer data to constrain it. The uncertainty for α_z increases steadily as the target location X coordinate increases. We interpret that the amount of Z axis magnetopause, which is being observed decreases steadily with X. The uncertainty on α_y increases only modestly or not at all. Over most of the interval the amount of Y axis magnetopause observed does not change very much.

Next we examine the reconstruction of the bow shock. In Figure 12b the reconstructed parameters r_0, α_y, and α_z do not vary with X. In Figure 12d we see that the uncertainties on r_0 and α_z decrease starting at about $X = 8 R_E$. Returning to Figure 11, we see that it is the point at which the bow shock boundary enters the image from the top. The improvement in the uncertainty on r_0 is a factor of 5, whereas the improvement is more modest for α_z. For α_y there is a modest increase in uncertainty, approximately a factor of 2, as X changes from 5 R_E to 13 R_E. We do not have an explanation for that variation.

5.4. Uniform Background Dependence

To determine how the reconstruction depends on the background, we carried out another experiment. We added a background to the images of known expectation value, which contributes to the photon noise in the images. We used average count of the model of 1 count per pixel (meaning that if the background counts are 1 count per pixel the average counts in the image with background is 2 counts per pixel). When the background is small, we expect no effect on the reconstruction. When it is comparable to, or greater than, the count rate from the model, we expect the reconstruction to degrade. We used the same viewing geometry (vantage point, target location, and image rotation) as in section 5.1. The uncertainties on the parameters r_0^{mp}, α_y^{mp}, and α_z^{mp} are shown in Figure 13a. The black curve is the standard deviation of the position of the magnetopause in units of Earth radii, the red curve is the standard deviation of α_y^{mp}, and the blue curve for α_z^{mp}. We see that reconstruction accuracy is independent of background count rate for backgrounds below 1 count per pixel. Above approximately 1 count per pixel of background the uncertainty increases, approximately as the square root of the background count level. For example, at 10 counts per pixel of background the uncertain has increase approximately by a factor of 3. In the case of α_y^{mp} and α_z^{mp} the results are approximately the same. In Figure 13b are shown the same results for the fitting of the bow shock. The results are the similar as for the magnetopause except that there is a little more noise in the curves for r_o^{bs} and α_y^{bs} and that the trend for α_z^{bs} is a little more steep; in this case the uncertainty increases by a factor of approximately 10, versus a factor of closer to 2 for the magnetopause. We do not have an explanation for the different
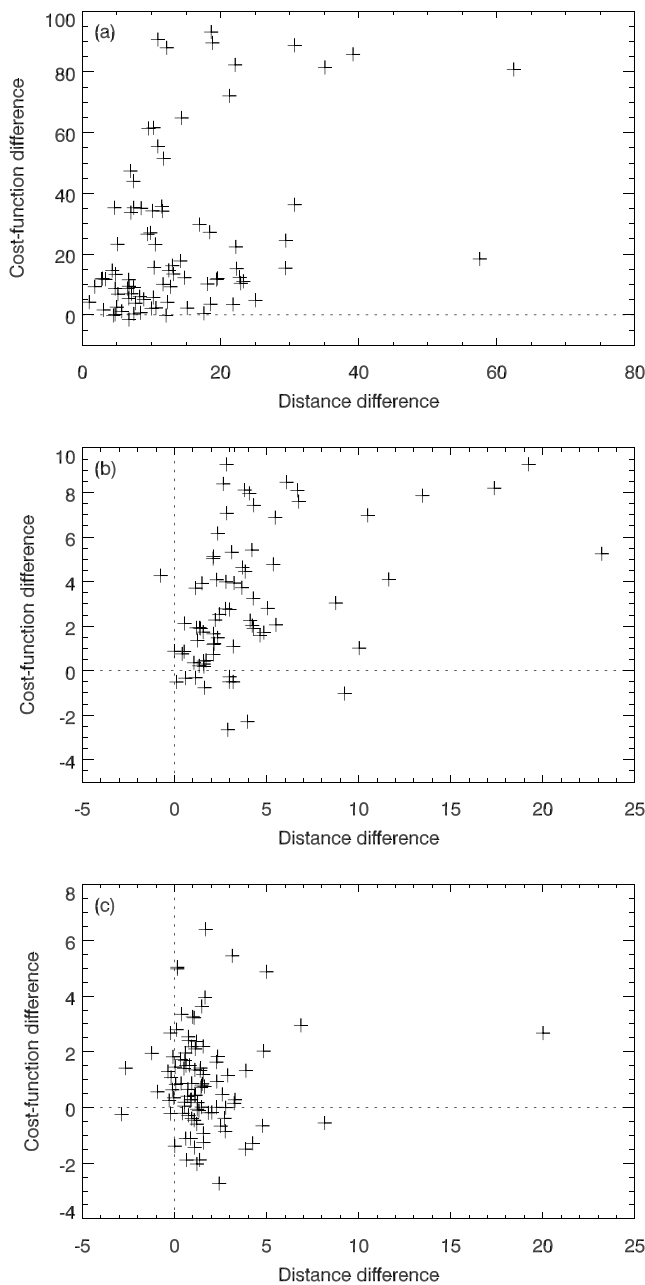
Figure 14. Depth of minimum of the random start fit minus depth of minimum of the true start fit plotted as a function of the distance difference (explained in the text) from the true parameters. (a–c) are for 1, 0.1, AND 0.01 count per pixel, respectively.

behavior of the uncertainty on α_z^{bs}, but one possibility is again to refer to a reviewer comment proposing that degeneracy among parameters can cause different uncertainty behavior as signal-to-noise ratio (SNR) decreases.

5.5. Fitting Algorithm Test

The Nelder and Mead simplex method (Nelder & Mead, 1965) is not a global minimization algorithm. The simplex follows a downhill path in the cost function landscape until it reaches a minimum, and it does not guarantee that it is the global minimum. To increase the likelihood that we do find the global minimum, we start the search at the known value of the parameter. Here we explore the extent to which that results in finding the global minimum. The experiment we carry out involves generating 100 images at each of three count levels, 1, 0.1, and 0.01 count per pixel.

One way to organize the result is to plot the depth of minima found from the random start minus the depth of minimum from start at the true value versus the distance from the true value. This is shown in Figure 14. Figures 14a–14c are for 1, 0.1, and 0.01 count per pixel, respectively. The horizontal axis shows the distance of the random start minimum from truth (R_r) minus the distance of the true start minimum from truth (R_t): $X = R_r - R_t$. The distance (R_r or R_t) is normalized in the following way. Along each of the 11 dimensions the fitted value minus the true value is divided by the root-mean-square (RMS) of the points that started at the true value. Then those values are summed in quadrature and divided by $\sqrt{11}$. The RMS distance of true start points is nominally 0, and a point on the horizontal axis at value x means that the random start point is x normalized distances further from the true point than the true starts fitted point. On the vertical axis is plotted random start cost function minimum minus the true start cost function minimum. If it is greater than 0, the true start found the deepest minimum. This is the situation that supports our method of using the true start to find the global minimum in the absence of a global minimization algorithm. If the method is not supported, we expect that half of the points fall below 0. We see that the method is working for 1 and 0.1 count per pixel and that it is showing signs of deteriorating at 0.01 count per pixel.

Another way to display the results is Figure 15 showing r_0^{bs} versus r_0^{mp} (2 of the 11 dimensions) for the three count rates, 1 per pixel in Figure 15a, 0.1 in Figure 15b, and 0.01 in Figure 15c. r_0^{mp} is the most important of the 11 parameters for the SMILE mission, which is why we choose to display it in the figure. In Figure 15 the filled circles are the found minima. A line connects the circles with the initial guess. The color of the circles indicates the depth of the minimum. The red circles are the 10% deepest minima, green the next 10% deepest minima, blue the next 10% deepest minima, and black the remaining 70%. By "depth of minimum" we mean the cost function minimum value reached by the random start minus the cost function minimum reached by the start at the known true point. The

value of the cost function minima reached fluctuates greatly from one random Poisson image to the next so the difference in minima organizes the data better. We see that for r_0^{mp} the fitting algorithm does find a point close to the true value for 1 and 0.1 count per pixel. For 0.01 count per pixel it is less clear. The deviation of the fitted parameters with randomized initial guesses tends to higher than those where the initial guess equals the true parameters. This suggests a complex cost function landscape with multiple false minima. The deviation is also larger at lower count rates. It is possible that cross correlation between some of the 11 parameters is the cause. Nonetheless, the deepest minimum is almost always close to the true parameters with possible exception of the lowest count rates. This suggests that a global minimization algorithm will be
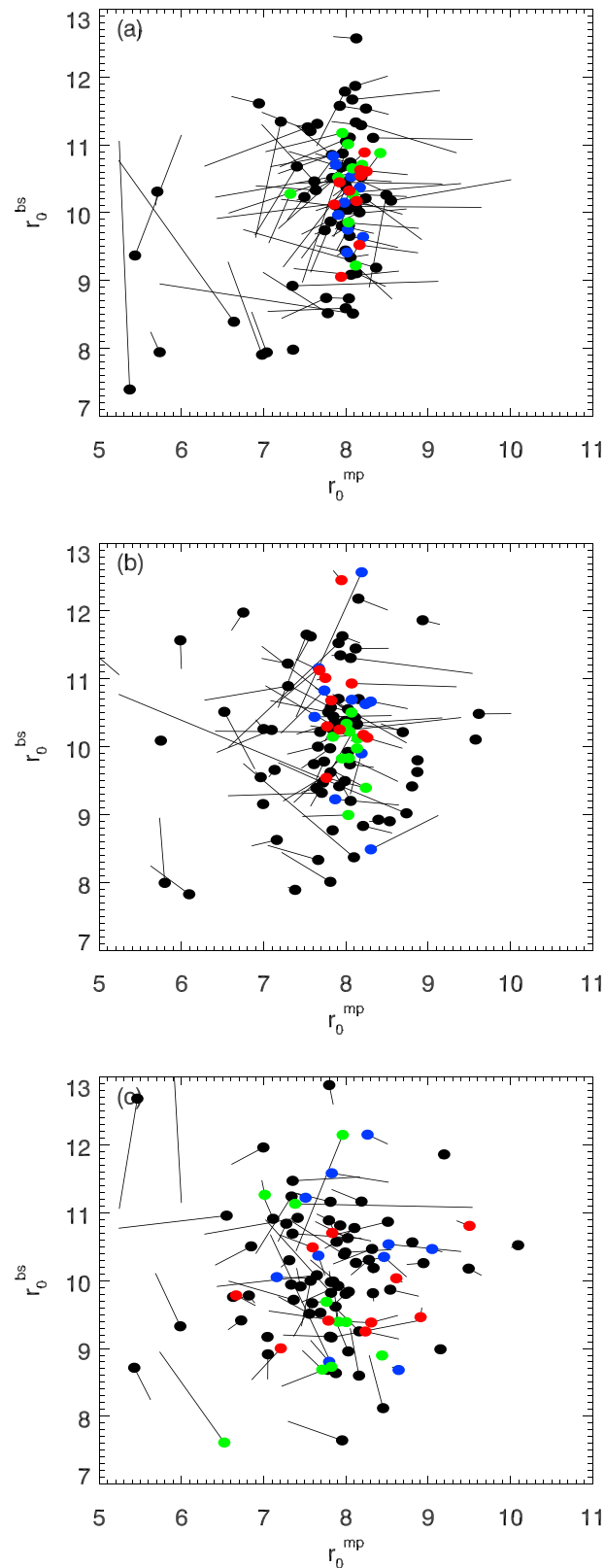
Figure 15. The value of r_0^{bs} versus r_0^{mp} for three 1, 0.1, and 0.01 count per pixel, in (a)–(c), respectively. The circles are the fitted end point, and the other end of the line is the starting point. The red points are the 10% deepest minima, the green the next 10% deepest minima, the blue the next 10% deepest minima, and the black points the 70% remaining minima.

able to find the correct parameters from a random starting point with the possible exception of the lowest count rates.

6. Discussion

The previous results suggest that it is indeed possible to reconstruct the three-dimensional structure of one or more boundaries from images, even for low count rates between 0.1 and 0.01 count per pixel under some circumstances. The specific circumstances in this paper are that the number of pixel data points must be much larger than the number of independent variables being fit and that the model must be able to exactly reproduce the observations in the image. This is true under a wide range of count rate conditions, background count rates, and viewing geometries.

However, we should emphasize the second assumption that the model must be capable of exactly reproducing the observations. This is very difficult to achieve with real data. This leads to a second type of uncertainty, which is related to the extent to which the model is capable of reproducing the observations. We call this fitting noise or fitting bias and can sometimes lead to unpredicted results in a fit. The reader is encouraged to consider the problem of fitting a straight line model to observations distributed according to a quadratic curve. The parameters extracted depends crucially on the distribution of data points which are fit. This problem is beyond the scope of the present paper, but it is the topic of a second paper which we are preparing.

It is well known that the astronomical X-ray background shows significant structure (Snowden et al., 1995). This means that the background count rate as well as its structure will depend on the look direction of the camera. While the average count rate is still a good guide for what can be expected in terms of SNR the actual X-ray background must be modeled accurately in observations in order to avoid it biasing boundary determinations.

In future work it may also be worthwhile to consider other functional forms for the boundaries as well as the brightness distribution in the magnetosheath and to a lesser extent the brightness distribution in the solar wind. Some of the ideas we have on that include functional forms, which are based on orthogonal function expansion, for example, a transformation of the basic forms according to multiplication by a function, which can be made progressively more sophisticated by adding terms. In the case of the SMILE observations such expansions are helped by the fact that the observations cover a relatively small segment of the magnetosheath and boundaries.

For the SMILE SXI camera coauthor Steve Sembay computed expected count rates from the SWCX mechanism as well as other mechanisms. These calculations have not yet been published in a refereed journal so are simply quoted here to provide context for the count rates expected. This calculation was done for a weak solar wind flux and a strong solar wind flux, for 0.5° pixel size. Since the pixel size we used in the rest of this paper are 0.2°, we have scaled the original calculations by a factor of $(2/5)^2$ in the following. The soft X-ray background count rate from non-SWCX sources (mainly diffuse emissions from the Galaxy) is 3.0×10^{-3} s^{-1}. The background count rate from local plasma is 1.3×10^{-3} s^{-1}. For weak solar wind flux, $n_{sw} u_{sw} = 2 \times 10^8$ cm^{-2}·s^{-1}, the SWCX peak count rate is 1.1×10^{-3} s^{-1}. Peak count rate occurs close to the subsolar point of the magnetopause. For strong solar wind flux, $n_{sw} u_{sw} = 1.5 \times 10^9$ cm^{-2}·s^{-1} the SWCX peak count rate is 16×10^{-3} s^{-1}. What these numbers translate to is total background counts of 0.26 in a 1-min integration and 1.3 in a 5-min integration in a 0.2° pixel. The peak foreground counts from SWCX for weak solar wind flux are 0.07 in a 1-min integration and 0.3 in a 5-min integration. Thus, the peak foreground counts are less than the average background counts in this case. This does not mean that the SNR is less than one for the purpose of extracting information from the image. As we saw above it is possible to extract information from the image even when the background counts are much larger than the foreground counts. For the case of strong solar wind flux the peak foreground counts are 1.0 for a 1-min integration and 4.8 in a 5-min integration, several times the background counts. In the calculations in the rest of this paper we plotted as a function of average foreground counts per pixel in the image. If we use the image in Figure 3 as typical we can convert from peak counts to average counts. In that image the peak counts is 1.6 times greater than the average counts. These results are summarized in Table 1. We can compare the values in the table with Figure 13. That figure assumes 1 count foreground. Thus, the case of weak solar wind flux corresponds to Figure 13 for a 20-min integration with 5 counts of background. The case of strong solar wind flux corresponds to Figure 13 for a 1-min integration with 0.3 counts of background. In both cases we are able to successfully reconstruct the bow shock and magnetopause.

Table 1
Expected Count Rates and Integrated Counts for 1, 5, and 20 min of Integration From the SWCX Foreground Source As Well As X-ray Sky Background and Particle Background

X-ray sources	s^{-1}	1 min	5 min	20 min
SWCX weak peak	1.1×10^{-3}	0.066	0.33	1.3
SWCX weak average	0.68×10^{-3}	0.04	0.20	0.82
SWCX strong peak	16×10^{-3}	1.0	4.8	19
SWCX strong average	10×10^{-3}	0.6	3.0	12
X-ray background	3.0×10^{-3}	0.18	0.90	3.6
Particle background	1.3×10^{-3}	0.08	0.39	1.6
Total background	4.3×10^{-3}	0.26	1.3	5.2

Note. The peak SWCX counts are the counts expected near the subsolar point of the magnetopause. The average counts are the counts averaged over an image with the viewing geometry of Figure 3. SWCX = solar wind charge exchange.

The typical solar wind conditions and integration times in Table 1 correspond to foreground counts per pixel of approximately 1 or more. This is a counts regime in which the fitting algorithm started at the truth point finds the global minimum in almost all cases. In that case the distribution of fitted points is an accurate representation of the distribution of the global minimum and the RMS of those an accurate representation of the standard uncertainty.

7. Conclusion

We have demonstrated that when the model is an exact representation of the observations and number of free model parameters are few, it is possible to reconstruct the three-dimensional structure of boundaries under a wide range of viewing geometries, backgrounds, and pixel count rates. The reconstruction accuracy obtained depends on pixel counts as expected, with the uncertainty on reconstructed parameters being proportional to pixel counts to the negative one-half power, in accordance with theoretical expectations. At lower count rates, the uncertainty becomes higher. The uncertainties obtained do depend on viewing geometries. Generally, the more of a boundary that is contained in the image, the smaller the uncertainty on the parameters of that boundary. Specifically, we found that the curvature of the magnetopause and bow shock boundaries in the direction along the viewing directions of the camera are better determined than those transverse to the boundaries.

Appendix A: Notes on Computation Implementation

All the fits presented in this paper were carried out on a cluster of four Dell M610 blade servers each containing two Intel Xeon X5680 CPUs each with 6 cores running at 3.33 GHz. Between the four servers 48 cores or 96 hyperthreads were available for the computation. The computation was parallelized, using the Message Passing Interface, at the pixel value integration level such that each thread computes approximately 100 pixels. Using hyperthreading at 96 threads provides a modest gain in computational speed versus using 48 threads, perhaps 20–30%. We found that computation scales extremely well between 1 and 48 threads (with a modest boost as we go from 48 to 96 hyperthreads). It takes approximately 2 min of wall clock time to fit one image with 11 free parameters, which corresponds to 96 min of CPU time. For each data point plotted in Figure 7 (13 counts per pixel), Figure 10 (13 spacecraft locations), Figure 12 (18 target locations), and Figure 13 (16 background levels) we did 100 Monte Carlo samples for a total of approximately 6,000 image fits corresponding to 8.5 days of wall clock time or 400 days of CPU time.

References

Carter, J., Sembay, S., & Read, A. (2010). A high charge state coronal mass ejection seen through solar wind charge exchange emission as detected by XMM–Newton. *Monthly Notices of the Royal Astronomical Society*, *402*(2), 867–878.

Collier, M. R., & Connor, H. K. (2018). Magnetopause surface reconstruction from tangent vector observations. *Journal of Geophysical Research: Space Physics*, *123*, 10,189–10,199. https://doi.org/10.1029/2018JA025763

Collier, M. R., Moore, T. E., Fok, M.-C., Pilkerton, B., Boardsen, S., & Khan, H. (2005). Low-energy neutral atom signatures of magnetopause motion in response to southward Bz. *Journal of Geophysical Research*, *110*, A02102. https://doi.org/10.1029/2004JA010626

Collier, M. R., Porter, F. S., Sibeck, D. G., Carter, J. A., Chiao, M. P., Chornay, D., et al. (2012). Prototyping a global soft X-ray imaging instrument for heliophysics, planetary science, and astrophysics science. *Astronomische Nachrichten*, *333*(4), 378–382.

Collier, M. R., Snowden, S., Sarantos, M., Benna, M., Carter, J. A., Cravens, T. E., et al. (2014). On lunar exospheric column densities and solar wind access beyond the terminator from ROSAT soft X-ray observations of solar wind charge exchange. *Journal of Geophysical Research: Planets*, *119*, 1459–1478. https://doi.org/10.1002/2014JE004628

Cravens, T. (1997). Comet Hyakutake X-ray source: Charge transfer of solar wind heavy ions. *Geophysical Research Letters*, *24*(1), 105–108.

Cravens, T. E. (2000). Heliospheric X-ray emission associated with charge transfer of the solar wind with interstellar neutrals. *The Astrophysical Journal Letters*, *532*(2), L153.

Cravens, T., Robertson, I., & Snowden, S. (2001). Temporal variations of geocoronal and heliospheric X-ray emission associated with the solar wind interaction with neutrals. *Journal of Geophysical Research*, *106*(A11), 24,883–24,892.

Hodges, R. R. (1994). Monte Carlo simulation of the terrestrial hydrogen exosphere. *Journal of Geophysical Research*, *99*(A12), 23,229–23,247.

Hu, Y., Guo, X., & Wang, C. (2007). On the ionospheric and reconnection potentials of the Earth: Results from global MHD simulations. *Journal of Geophysical Research*, *112*, A07215. https://doi.org/10.1029/2006JA012145

Jorgensen, A. M. (2018). Boundary detection in three dimensions with application to the smile mission: The effect of photon noise. http://osf.io/r5jbg

Kronrod, A. S. (1965). Nodes and weights of quadrature formulas.

Lisse, C., Dennerl, K., Englhauser, J., Harden, M., Marshall, F., Mumma, M., et al. (1996). Discovery of X-ray and extreme ultraviolet emission from comet C/Hyakutake 1996 B2. *Science*, *274*(5285), 205–209.

Nelder, J. A., & Mead, R. (1965). A simplex method for function minimization. *The Computer Journal*, *7*(4), 308–313.

Peele, A. G., Lyngsjo, H., Crocker, R. M., Markham, J., Bannister, N., & Nugent, K. A. (2004). Modeling of the Lobster-ISS X-ray telescope in orbit, *UV and gamma-ray space telescope systems* (Vol. 5488, pp. 232–242). Glasgow, Scotland: International Society for Optics and Photonics.

Raab, W., Branduardi-Raymont, G., Wang, C., Dai, L., Donovan, E., Enno, G., et al. (2016). Smile: A joint ESA/CAS mission to investigate the interaction between the solar wind and Earth's magnetosphere, *Space telescopes and instrumentation 2016: Ultraviolet to gamma ray* (Vol. 9905, pp. 990502).Edinburgh, Scotland: International Society for Optics and Photonics.

Robertson, I., Collier, M., Cravens, T., & Fok, M.-C. (2006). X-ray emission from the terrestrial magnetosheath including the cusps. *Journal of Geophysical Research*, *111*, A12105. https://doi.org/10.1029/2006JA011672

Robertson, I. P., & Cravens, T. E. (2003). X-ray emission from the terrestrial magnetosheath. *Geophysical Research Letters*, *30*(8), 1439. https://doi.org/10.1029/2002GL016740

Russell, C. T. (1971). Geophysical coordinate transformations. *Cosmic Electrodynamics*, *2*(2), 184–196.

Shue, J.-H., Chao, J., Fu, H., Russell, C., Song, P., Khurana, K., & Singer, H. (1997). A new functional form to study the solar wind control of the magnetopause size and shape. *Journal of Geophysical Research*, *102*(A5), 9497–9511.

Snowden, S., Collier, M., Cravens, T., Kuntz, K., Lepri, S., Robertson, I., & Tomas, L. (2009). Observation of solar wind charge exchange emission from exospheric material in and outside Earth's magnetosheath 2008 September 25. *The Astrophysical Journal*, *691*(1), 372.

Snowden, S., Freyberg, M., Plucinsky, P., Schmitt, J., Trümper, J., Voges, W., et al. (1995). First maps of the soft X-ray diffuse background from the ROSAT XRT/PSPC all-sky survey. *The Astrophysical Journal*, *454*, 643.

Sun, T., Wang, C., Wei, F., & Sembay, S. (2015). X-ray imaging of Kelvin-Helmholtz waves at the magnetopause. *Journal of Geophysical Research: Space Physics*, *120*, 266–275. https://doi.org/10.1002/2014JA020497